JCIM JOURNAL OF CHEMICAL INFORMATION AND MODELING

pubs.acs.org/jcim Article

Thermal Stability of Hollow Porous Gold Nanoparticles: A Molecular Dynamics Study

Felipe J. Valencia,* Max Ramírez, Alejandro Varas, José Rogan, and Miguel Kiwi

Cite This: J. Chem. Inf. Model. 2020, 60, 6204−6210 Read Online

ACCESS | Metrics & More | Article Recommendations

ABSTRACT: Hollow nanoparticle structures play a major role in nanotechnology and nanoscience since their surface to volume ratio is significantly larger than that of filled ones. While porous hollow nanoparticles offer a significant improvement of the available surface area, there is a lack of theoretical understanding, and scarce experimental information, on how the porosity controls or dominates the stability. Here we use classical molecular dynamics simulations to shed light on the particular characteristics and properties of gold porous hollow nanoparticles and how they differ from the nonporous ones. Adopting gold as a prototype, we show how, as the temperature increases, the porosity introduces surface stress and minor transitions that lead to various scenarios, from partial shrinkage for small filling factors to abrupt compression and the loss of spherical shape for large filling. Our work provides new insights into the stability limits of porous hollow nanoparticles, with important implications for the design and practical use of these enhanced geometries.

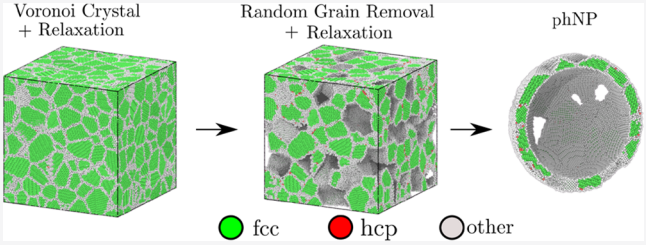

INTRODUCTION

The synthesis of porous hollow nanoparticles (phNPs) has attracted much attention due to the scientific interest they raised and the many possible applications they make feasible.[1−5] phNPs are now obtained by several simple and rapid methods. Wang et al.[6] synthesized hollow nanocrystals through the nanoscale Kirkendall effect. Nguyen-Thi et al.[7] engineered porous silica and hollow silica nanoparticles (NPs). Jayaprakash et al.[8] obtained hollow porous carbon−sulfur composites for power lithium sulfur batteries in 2011. Hu et al.[9] synthesized colloidal porous gold nanoparticles, while Hakimian et al.[10] developed a simple and rapid method to fabricate porous gold nanoparticles.

All of the above opened the way for a whole wealth of possible new applications.[11−13] The large surface to volume ratio and low density of phNPs are the additional ingredients that make them superior to solid and perfect hollow nanoparticles. This geometry presents a challenge for both basic research and novel applications since they can be used in many types of reactors, for catalysis, drug delivery, storage devices, and the development of novel lightweight materials.[14−19]

However, these experimental achievements have not been accompanied by much theoretical work, which has been focused only on perfect hollow nanostructures[20−23] rather than on phNPs, which are the ones prevalent when the various synthesis methods are implemented. It is worth noticing that while a porouslike nanostructure has been proposed as an alternative to improve the performance of hollow NPs, there is little quantitative experimental characterization available on these systems.[2,24−27] Therefore, many of the experimental results obtained should be interpreted considering the properties of these nanoparticles. Recently, classical molecular dynamics simulations have shown that defect inclusion, particularly in grain boundary structures, plays a significant role in the stability of hollow nanoparticles (hNPs).[28] To achieve more realistic scenarios and to determine the limitations of phNP, we report molecular dynamics simulations intended to develop an understanding of the unique phNP characteristics and properties and establish how they differ from nonporous hNPs. We focus our interest in gold nanoparticles, on which a simple synthesis method with a temperature-controlled diameter and pore sizes became recently available.[24−27,29−31] This contribution constitutes a generalization of the theoretical work on gold NPs and hNPs, which using similar techniques has already been published.[20,21,32−34] However, to the best our knowledge, this is the first work on porouslike shells.

METHODS

In order to shed light on the understanding of the special characteristics and properties of phNPs, we performed

Received: July 9, 2020
Published: October 29, 2020

https://dx.doi.org/10.1021/acs.jcim.0c00785
J. Chem. Inf. Model. 2020, 60, 6204−6210

Molecular Dynamics simulations[35−37] using the LAMMPS code.[38] The embedded-atom method[39] potential with the parametrization developed by Sheng et al.[40] was used to simulate the Au atom interactions. While several potentials can be employed to model hollow nanoparticles, the EAM community has used it to simulate hollow Pt, Ag, Au, and Pd nanostructures, among many other examples.[20,22,23,33,41−44] In particular, the Sheng et al.[40] EAM parametrization fits a variety of physical properties such as lattice dynamics, mechanical properties, thermal behavior, energetics of competing crystal structures, defects, deformation paths, liquid structures, and so forth.

Because of their improved accuracy and wide applicability, these potentials are most suitable for high-quality atomistic computer simulation of finite systems, such as the ones we investigate here.[45]

To build the initial phNP, we carved a thick spherical shell from polycrystalline bulk. This process has four consecutive steps, which are illustrated in Figure 1 and are described below.

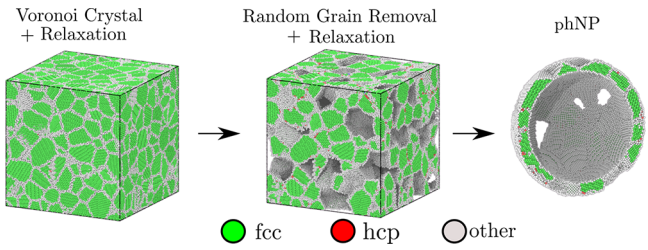

Figure 1. Scheme of the phNP construction: we start with a 5 nm average grain size Voronoi polycrystal. Once the sample is relaxed, grains are removed at random. Finally, a phNP is constructed cutting two concentric spheres from the porous nanocrystal; the resulting nanostructure has a 10 nm radius and a thickness of 2.5 nm. The color coding indicates the crystal structure, according to the common neighbor analysis algorithm. Green atoms, fcc; red atoms, hcp; white, other.

1. We construct a polycrystalline Au bulk, with a given average grain size, using a Voronoi tessellation algorithm.[46−48] The Au polycrystalline bulk consists of a cell of 28 nm × 28 nm × 28 nm with 355 randomly oriented grains and an average grain size of 5 nm. As the resulting polycrystal is probably out of equilibrium, an exhaustive relaxation of the system is carried out. Initially, the grain boundaries are very close to each other; therefore, the atoms with energies larger than 10 eV are removed from the polycrystal. The structure is then relaxed using the energy-minimization conjugate-gradient algorithm, along with the box/relax algorithm; both are implemented in the LAMMPS code. The first algorithm allows the polycrystal to reach a local minimum energy. The second one eliminates any excess pressure introduced during the process. To allow grain boundaries to freely accommodate and to avoid spurious high-energy grain boundaries, the temperature is raised to $2T_{bm}/3$ with a barostat at zero pressure, where T_{bm} is the bulk melting temperature. This procedure is carried out during 20−50 ps, and the system is next cooled back to 10 K. This way, we ensure that the remaining polycrystal pressure is smaller than 10^{-5} GPa.
2. To construct the phNP, a given number of grains are randomly removed from the relaxed polycrystal. As a consequence of the porosity, the system could be out of equilibrium due to internal stresses induced by the large number of holes; thus, the system is relaxed once again, with the conjugated gradient and the box/relax algorithm. Then, to equilibrate the porous polycrystal, the system temperature is carried to 300 K using a Nose−Hover thermostat. The temperature is raised during 0.2 ns, using a 1.0 fs time step. The system is coupled to a zero pressure barostat to dissipate residual stresses during grain boundary accommodation.
3. Once the system is relaxed, the phNP is constructed by carving two concentric spheres from the porous nanocrystal, with an inner and outer radius of 7.5 and 10 nm, respectively. These radii were selected since previous work has shown that Au hollow nanoparticles of these sizes (single crystal and polycrystalline) are thermally stable, which allows us to choose proper radii and thicknesses[20,28] above 300 K.
4. The resulting porous hollow nanospheres are finally relaxed using a conjugate gradient algorithm and later equilibrated by raising the temperature to 300 K during 0.5 ns, with a 1.0 fs time step. The temperature was controlled with a velocity rescaling algorithm implemented in the LAMMPS code.

We note that the resulting structure corresponds to a phNP with grain boundary structure and holes, in agreement with the experimental evidence. The phNP porosity was characterized by the filling factor ϕ, which is defined as

$$\phi = V/V_0 \tag{1}$$

where V is the volume occupied by the atoms of the phNP and V_0 the volume of the phNP with no pores. The volume V was computed using the construct surface mesh algorithm implemented in OVITO,[49,50] with a probe sphere consistent with the first-neighbor distance of the Au lattice. For a statistical analysis we performed simulations with 50 different porosity values (by deleting a given number of grains during the second step of the phNP construction), in the range of ϕ = 0.58 to ϕ = 1.00. Smaller filling factors turned out to be thermally unstable and therefore are not included.[20] Crystalline structure recognition was performed by means of the common neighbor analysis algorithm.[51]

The thermal stability for the 50 phNP was determined by raising the system temperature by means of a velocity rescaling algorithm. The temperature is increased in 20 K intervals during 400 ps, using a 2.0 fs time step. Averages are calculated during the last 50 ps for each temperature. The structure recognition, visualization, and postprocessing were performed employing the OVITO software.[49,50]

RESULTS AND DISCUSSION

The thermal stability of NPs is not affected for temperatures below several hundred Kelvin. However, for hNPs the scenario is quite different; the inner cavity introduces surface effects that make the nanostructure prone to collapse under particular thermal conditions, limiting their potential applications. For phNPs the increase in the surface area not only improves the exceptional surface-to-volume ration of hNPs but also introduces surface stresses which might compromise the phNP thermal stability. In Figure 2 we display different potential energy curves as a function of temperature. At high temperatures the porosity does not play a significant role in

https://dx.doi.org/10.1021/acs.jcim.0c00785
J. Chem. Inf. Model. 2020, 60, 6204−6210

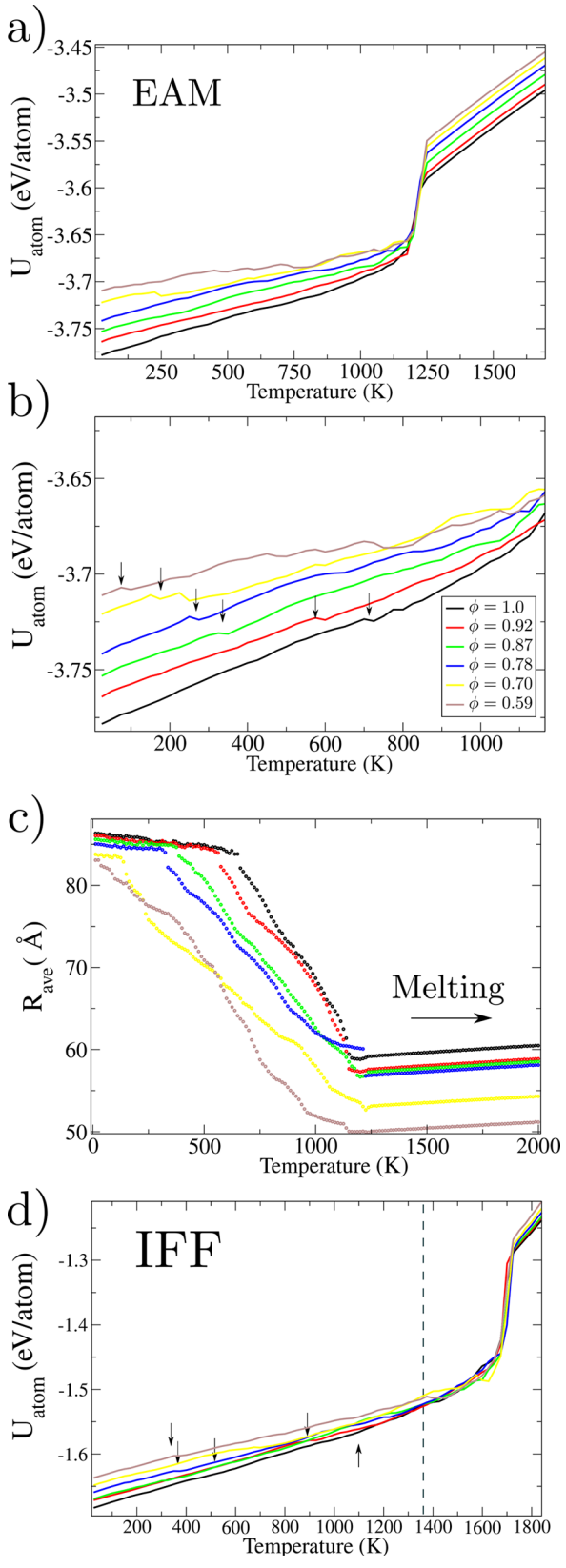

Figure 2. (a) Per-atom potential energy U as a function of temperature for different ϕ values; the abrupt increase at $T \approx 1250$ K identifies the melting temperature. (b) Low-temperature region; the arrows indicate small potential energy drops. (c) Average radius of the phNP as a function of temperature. (d) Per-atom potential energy as a temperature function using the IFF potential. The inset in (b) applies to panels (a), (c), and (d).

modifying the melting point, where the shift in T_m goes from 1240 K for $\phi = 1.0$ to 1220 K for $\phi = 0.58$. This reduction is mainly attributed to the surface area increase due to the large number of pores, which may lead to enhanced surface diffusion. The aforementioned analysis does not reveal significant differences in collapse temperature, apart from the melting point shift of the phNP. Interestingly, a close inspection of low-temperature ($T \leq 700$) K potential energy curves (Figure 2b) clearly shows small "jumps" that take place even below the melting temperature (T_m). Often in NPs the potential energy grows linearly with T, without fluctuations; here those jumps are strongly related to structural transformation events of the phNP. As can be observed, the hNP does not show significant fluctuations for $\phi = 1.0$ until $T \sim 500$ K is reached, a scenario that changes with increasing porosity. For smaller filling factors those jumps are more frequent as the temperature increases. Generally the reduction of the potential energy U is related to a small transition, which alleviates surface stress. In Figure 2c it is shown that the small steps correspond to partial shrinkage of the phNP; in fact, a radius decrease can be observed even for temperatures below room temperature, as is the case for filling factors $\phi < 0.59$. To test if our results are reliable, we also performed the same simulations using the interface force field (IFF) potential.[52] This force field is highly optimized for surface and interface energies yielding an error <3% for the Au surface energy and has been successfully employed in diverse scenarios.[53−56] The thermal loading curve displayed in Figure 2d shows a similar tendency with porosity as reported for the Sheng potential.[45] Also, small jumps associated with partial shrinkage are observed before the phNP collapses, suggesting as expected that the partial collapse is due to thermal effects and not to the choice of the interatomic potential. The major differences do occur for melting temperatures where IFF renders a phNP melting larger than the bulk melting point (vertical dashed line in Figure 2d). The high melting point of the IFF Au potential has been reported recently for nanoclusters of a few atoms.[57] It is worthwhile to notice that Sheng et al.[40] renders a 25% error on Au surface energies; however, EAM reproduces reasonably well the mechanical properties, elastic constants, melting point, and the generalized stacking fault energies with errors smaller than a %5 with respect to experimental measurements and DFT calculations.[58,59] Since EAM reproduces successfully several physical quantities with an acceptable error range and has been widely used in the literature for the modeling of metallic hollow nanostructures,[22,33,42,43] the following analyses were performed with the Sheng EAM potential.[45]

Figure 3 depicts the temperature dependent shrinkage process for three different porosity values. For $\phi = 1.0$ the conventional hNP shrinks slightly during the first 300 K; this is consistent with grain boundary accommodation and stress release due to the nucleation of several partial Shockley dislocations, which take place to reduce surface tension.[20,33,60] For $\phi = 0.78$ the structure reaches an intermediate state, between a thermal resistant structure for $\phi = 1.0$ and a highly porous and unstable structure for $\phi = 0.59$. The increase in porosity enhances surface effects, which often trigger the healing of small pores at low temperatures. Although these effects accomplish a size decrease, the phNP readily stabilizes, and no further modifications take place at temperatures larger than $T \approx 300$ K. For $\phi = 0.59$ the scenario is rougher, since the continuous porous closure does occur in many regions over the hNP shell, leading to an abrupt compression and the loss of the

https://dx.doi.org/10.1021/acs.jcim.0c00785
J. Chem. Inf. Model. 2020, 60, 6204−6210

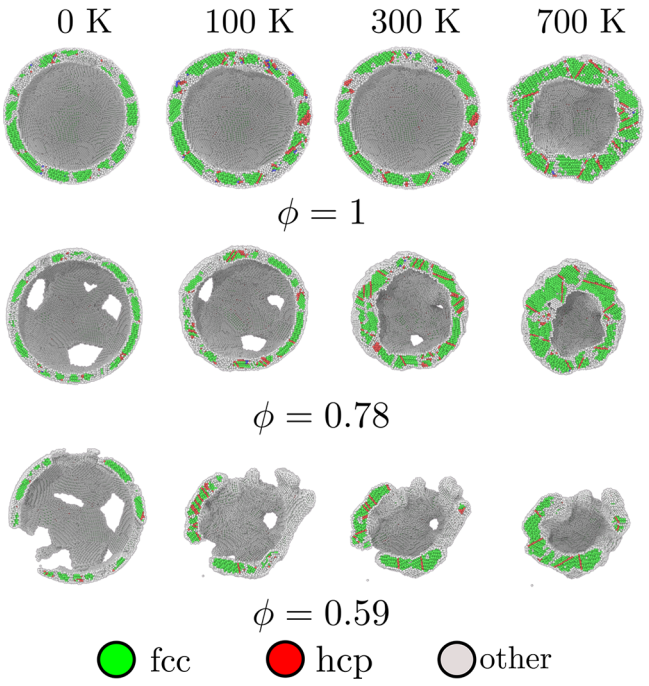

Figure 3. Three representative phNP for several temperatures. Atoms are colored according to their crystalline structure; green, red, and white correspond to fcc, hcp, and other, respectively.

characteristic spherical shape. In some cases filaments break away; in other cases, amorphization is observed in the large pore concentration regions. The continuous filament sintering has already been observed in phNP synthesized by plasma etching,[31] where the plasma flow is used to tune the filament size. While those Au phNP are much larger than the ones here simulated, the underlying mechanism is the same; temperature enhances surface diffusion, leading to the sintering of phNP grains. It is interesting to note that pore size is often used as a route to tune catalytic activity or plasmonic resonance.[2,24,27,61] While larger porous structures are desirable to obtain better performance, it is shown here that thermal effects decrease the pore size and, therefore, the performance for such applications. In plasmonic resonance, the electronic excitations are coupled with the lattice to lead to the nanostructure heating. The introduction of a highly porous structure, for $\phi = 0.6$, does lead to nanoparticles with low cyclic performance, since the loss of the porouslike structures is expected after several thermal cycles.

To characterize the impact of porosity on the phNP stability, several structures were studied as a function of the filling factor ϕ. Figure 4 provides results for 50 phNPs studied, for temperatures up to 700 K, where the dots correspond to the temperature of the first structural collapse or shrinkage suffered by the phNP. To classify them we employed the definitions by Jiang et al.[20] which label as stable a hNP that maintains its spherical geometry, without suffering further modifications; instead, labeled as half-stable is a hNP which partially collapses but does maintain its hollow structure. Interestingly, in Figure 4 it is straightforward to notice the large dispersion of the first temperature collapse of the different phNPs. This result can be attributed to the random algorithm used to remove grains of the initial polycrystalline sample. In some cases, two or more neighboring (or close by) grains could be removed, leading to

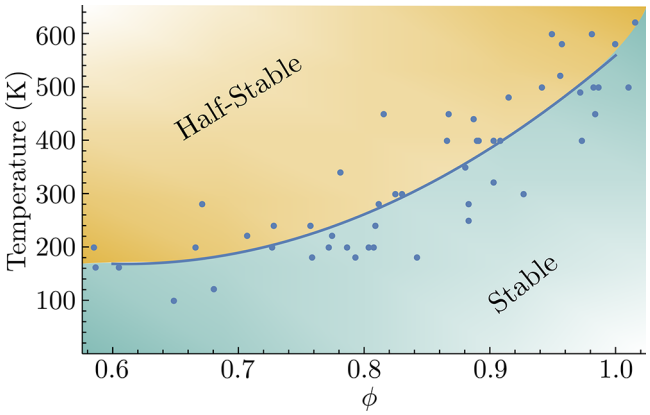

Figure 4. Phase diagram of the stable to half-stable transition as a function of the filling factor ϕ. The continuous line corresponds to a quadratic fit of the data given by $T = 1330.2 + 2931.5\phi^2$.

small filaments or high-energy surfaces, which are prone to collapse when the temperature is progressively increased.

We observe a progressive increase in the stability threshold as a function of porosity. As $\phi \to 1.0$, the collapse temperature increases quadratically with porosity. It is worth noticing that hNPs with porosities less than $\phi = 0.8$ establish the limit for room temperature stability, at least for the geometrical parameters chosen here. For lower ϕ values the phNP simply collapses, reducing the size and the structure porosity and leading to a final structure which deviates from those which are desirable. The collapse temperature increase seems to follow a quadratic law with porosity. Our explanation is based on the fact that the surface area increases quadratically with the filling factor, increasing the surface stress and enabling additional sites potentially active for the nucleation of partial dislocations.

For the stability we compare the single-atom energy relative to the polycrystalline NP and the phNP. The excess energy is defined as the difference between the single-atom potential energy of a phNP and the single-atom energy of a polycrystal bulk. The per-atom potential energy of the polycrystalline bulk is 3.88 eV/atom and was obtained from the relaxed polycrystal used to construct the phNP. The plot of the excess energy in Figure 5a shows a linear decrease with the filling factor ϕ, while the non-phNP ($\phi = 1.0$) shows an excess energy of 0.072 eV/atom compared to the nanocrystal bulk. As ϕ decreases the excess energy increases linearly, suggesting that the porous structure deviates from the $\phi = 1$ local minimum. Interestingly, the single-atom excess energy, between $\phi = 1.0$ and $\phi = 0.58$, is not larger than 0.05 eV/atom; this difference can be achieved by means of thermal effects, for temperatures up to ~500 K. Consequently, phNP with larger ΔU are likely to become unstable when the temperature is increased (see Figure 5b). The excess energy to ensure a stable structure, at least at room temperature, is 0.9 eV/atom. Larger values tend to be strongly sensitive to thermal variations, and even to collapse at temperatures below those required for practical or industrial applications.

CONCLUSIONS

The successful synthesis of hollow nanoparticles has opened new possibilities for many applications and generated basic questions about their properties. In particular, the role displayed by their intrinsic defects, as grain boundaries or pores, has been scarcely studied yet. Here we report the results

https://dx.doi.org/10.1021/acs.jcim.0c00785
J. Chem. Inf. Model. 2020, 60, 6204−6210

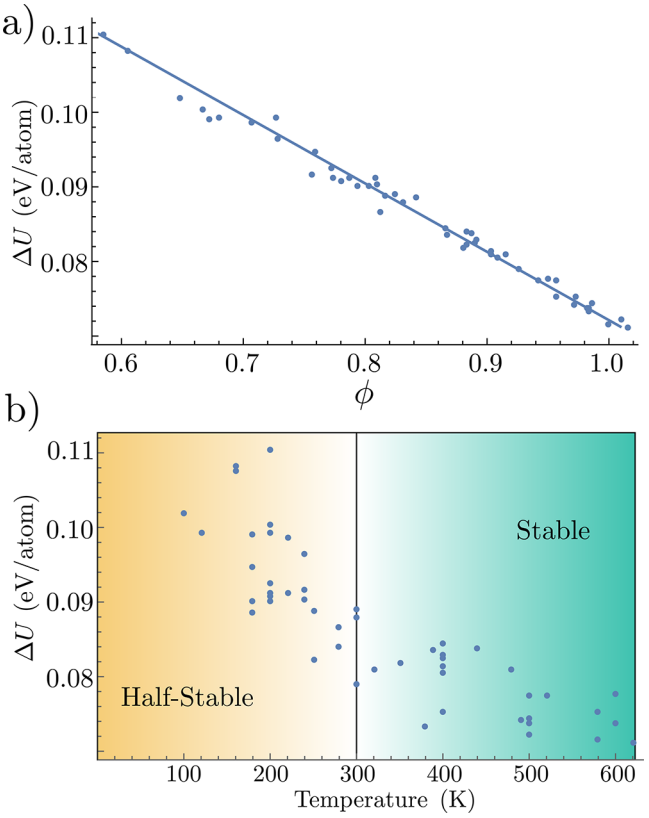

Figure 5. (a) Excess energy (ΔU) as a function of the filling factor ϕ. (b) Excess energy as a function of the temperature of the stable to half-stable transition. The vertical line sets the boundary between the two regions.

of molecular dynamics simulations of the thermal stability of gold porous hollow nanoparticles (phNPs). Our results show that porosity plays a major role in the thermal stability of the structures we investigated, a variable that, as far as we know, has not been included in previous modeling of hollow nanostructures. In particular, porosity considerably reduces the stable to half-stable transition temperature of phNPs; therefore, it should be considered when contrasting experimental data (which habitually includes, due to synthesis methods, phNPs) with theoretical stability predictions almost always computed for perfect hNPs. In addition, we notice that all the nanostructures we simulated maintain almost the same melting point. However, the phNP shrinkage strongly depends on the temperature and porosity of the nanoparticle. We attribute this effect to the increase of the surface-to-volume ratio, which enhances surface effects and leads to phNP partial collapse, mediated by stacking faults and partial dislocations. For the nanostructures simulated, we found that a filling factor of 0.85 yields stable phNPs for temperature higher than 300 K, a key feature for possible applications. Smaller filling factors increase the excess energy and consequently the surface tension, which is responsible for size decrease and/or shrinkage. Also, partial collapse assisted by pore healing and radius decrease does appear, even at temperatures of a few Kelvin. All in all, our study and methodology provide encouraging results and emphasize the importance of including defects in theoretical calculations, as well as a scheme to study other porous hollow nanoparticles and porous nanostructures in general. Future work may study more complex scenarios, such as the inclusion of solvents with different pH concentrations; they certainly will play a role in the hollow nanostructure stabilization process. In addition, we expect that our model can be used to treat more complex nanoparticles, such as porous nanoboxes, prisms, or starlike nanostructures.

AUTHOR INFORMATION

Corresponding Author

Felipe J. Valencia − *Centro de Investigación DAiTA Lab, Facultad de Estudios Interdisciplinarios, Universidad Mayor, Santiago, Chile; Centro para el Desarrollo de la Nanociencia y la Nanotecnología, CEDENNA, Santiago, Chile 9170124;* orcid.org/0000-0002-5461-6885; Email: felipe.valenciad@gmail.com

Authors

Max Ramírez − *Departamento de Física, Facultad de Ciencias, Universidad de Chile, Santiago, Chile 7800024; Centro para el Desarrollo de la Nanociencia y la Nanotecnología, CEDENNA, Santiago, Chile 9170124*

Alejandro Varas − *Departamento de Física, Facultad de Ciencias, Universidad de Chile, Santiago, Chile 7800024; Centro para el Desarrollo de la Nanociencia y la Nanotecnología, CEDENNA, Santiago, Chile 9170124*

José Rogan − *Departamento de Física, Facultad de Ciencias, Universidad de Chile, Santiago, Chile 7800024; Centro para el Desarrollo de la Nanociencia y la Nanotecnología, CEDENNA, Santiago, Chile 9170124*

Miguel Kiwi − *Departamento de Física, Facultad de Ciencias, Universidad de Chile, Santiago, Chile 7800024; Centro para el Desarrollo de la Nanociencia y la Nanotecnología, CEDENNA, Santiago, Chile 9170124;* orcid.org/0000-0001-8580-1912

Complete contact information is available at: https://pubs.acs.org/10.1021/acs.jcim.0c00785

Notes

The authors declare no competing financial interest.

ACKNOWLEDGMENTS

This work was supported by the Fondo Nacional de Investigaciones Científicas y Tecnológicas (FONDECYT, Chile) under grants #1190662 (J.R., M.K., M.R., A.V., F.J.V) and FONDECYT de Iniciación #11190484 (F.J.V.). The authors thank the Financiamiento Basal para Centros Científicos y Tecnológicos de Excelencia AFB180001. This research was partially supported by the supercomputing infrastructure of the NLHPC (ECM-02).

REFERENCES

(1) Cho, Y.-B.; Kim, J. E.; Shim, J. H.; Lee, C.; Lee, Y. Synthesis and Electrocatalytic Cctivity of Highly Porous Hollow Palladium Nanoshells for Oxygen Reduction in Alkaline Solution. *Phys. Chem. Chem. Phys.* **2013**, *15*, 11461−11467.

(2) Wu, H.; Wang, P.; He, H.; Jin, Y. Controlled Synthesis of Porous Ag/Au Bimetallic Hollow Nanoshells with Tunable Plasmonic and Catalytic Properties. *Nano Res.* **2012**, *5*, 135−144.

(3) Wang, Y.; Kong, A.; Chen, X.; Lin, Q.; Feng, P. Efficient Oxygen Electroreduction: Hierarchical Porous Fe−N-doped Hollow Carbon Nanoshells. *ACS Catal.* **2015**, *5*, 3887−3893.

(4) Yu, W.; Jiang, X.; Ding, S.; Li, B. Preparation and Electrochemical Characteristics of Porous Hollow Spheres of NiO Nanosheets as Electrodes of Supercapacitors. *J. Power Sources* **2014**, *256*, 440−448.

(5) Si, Y.; Chen, M.; Wu, L. Syntheses and biomedical applications of hollow micro-/nano-spheres with large-through-holes. *Chem. Soc. Rev.* **2016**, *45*, 690−714.
(6) Wang, W.; Dahl, M.; Yin, Y. Hollow Nanocrystals through the Nanoscale Kirkendall Effect. *Chem. Mater.* **2013**, *25*, 1179.
(7) Nguyen-Thi, N.-T.; Tran, L. P. P.; Le, N. T. T.; Cao, M.-T.; Tran, T.-N.; Nguyen, N. T.; Nguyen, C. H.; Nguyen, D.-H.; Than, V. T.; Le, Q. T.; Trung, N. Q. The Engineering of Porous Silica and Hollow Silica Nanoparticles to Enhance Drug-loading Capacity. *Processes* **2019**, *7*, 805.
(8) Jayaprakash, N.; Shen, J.; Moganty, S. S.; Corona, A.; Archer, L. A. Porous Hollow Carbon@Sulfur Composites for High-Power Lithium-Sulfur Batteries. *Angew. Chem., Int. Ed.* **2011**, *50*, 5904.
(9) Hu, J.; Jiang, R.; Zhang, H.; Guo, Y.; Wang, J.; Wang, J. Colloidal Porous Gold Nanoparticles. *Nanoscale* **2018**, *10*, 18473.
(10) Hakimian, F.; Ghourchian, H. Simple and Rapid Method for Synthesis of Porous Gold Nanoparticles and its Application in Improving DNA Loading Capacity. *Mater. Sci. Eng., C* **2019**, *103*, 109795.
(11) Suh, W. H.; Suslick, K. S. Magnetic and Porous Nanospheres from Ultrasonic Spray Pyrolysis. *J. Am. Chem. Soc.* **2005**, *127*, 12007−12010.
(12) Zhou, W.; Wang, C.; Zhang, Q.; Abruña, H. D.; He, Y.; Wang, J.; Mao, S. X.; Xiao, X. Tailoring Pore Size of Nitrogen-doped Hollow Carbon Nanospheres for Confining Sulfur in Lithium−Sulfur Batteries. *Adv. Energy Mater.* **2015**, *5*, 1401752.
(13) Yang, W.; Mao, S.; Yang, J.; Shang, T.; Song, H.; Mabon, J.; Swiech, W.; Vance, J. R.; Yue, Z.; Dillon, S. J.; et al. Large-Deformation and High-Strength Amorphous Porous Carbon Nanospheres. *Sci. Rep.* **2016**, *6*, 24187.
(14) Cheng, K.; Peng, S.; Xu, C.; Sun, S. Porous Hollow Fe3O4 Nanoparticles for Targeted Delivery and Controlled Release of Cisplatin. *J. Am. Chem. Soc.* **2009**, *131*, 10637−10644.
(15) Shervani, S.; Mukherjee, P.; Gupta, A.; Mishra, G.; Illath, K.; Ajithkumar, T.; Sivakumar, S.; Sen, P.; Balani, K.; Subramaniam, A. Multi-mode Hydrogen Storage in Nanocontainers. *Int. J. Hydrogen Energy* **2017**, *42*, 24256−24262.
(16) Gupta, A.; Shervani, S.; Rani, P.; Sivakumar, S.; Balani, K.; Subramaniam, A. Hybrid Hollow Structures for Hydrogen Storage. *Int. J. Hydrogen Energy* **2020**, *45*, 24076−24082.
(17) Ghosh, P.; Han, G.; De, M.; Kim, C. K.; Rotello, V. M. Gold Nanoparticles in Delivery Applications. *Adv. Drug Delivery Rev.* **2008**, *60*, 1307.
(18) Hwang, S. H.; Yun, J.; Jang, J. Multi-Shell Porous TiO2 Hollow Nanoparticles for Enhanced Light Harvesting in Dye-sensitized Solar Cells. *Adv. Funct. Mater.* **2014**, *24*, 7619−7626.
(19) Gupta, A.; Shervani, S.; Amaladasse, F.; Sivakumar, S.; Balani, K.; Subramaniam, A. Enhanced Reversible Hydrogen Storage in Nickel Nano Hollow Spheres. *Int. J. Hydrogen Energy* **2019**, *44*, 22032−22038.
(20) Jiang, L.; Yin, X.; Zhao, J.; Liu, H.; Liu, Y.; Wang, F.; Zhu, J.; Boey, F.; Zhang, H. Theoretical Investigation on the Thermal Stability of Hollow Gold Nanoparticles. *J. Phys. Chem. C* **2009**, *113*, 20193−20197.
(21) Jiang, L.; Sun, W.; Gao, Y.; Zhao, J. Geometric Thermal Phase Diagrams for Studying the Thermal Dynamic Stability of Hollow Gold Nanoballs at Different Temperatures. *Phys. Chem. Chem. Phys.* **2014**, *16*, 6623−6629.
(22) Dalgic, S. S. Size Dependent Properties of Hollow Gold Nanoparticles: A Theoretical Investigation. *Acta Phys. Pol., A* **2016**, *129*, 531−534.
(23) Huang, R.; Shao, G.-F.; Zeng, X.-M.; Wen, Y.-H. Diverse Melting Modes and Structural Collapse of Hollow Bimetallic Core-Shell Nanoparticles: A Perspective from Molecular Dynamics Simulations. *Sci. Rep.* **2015**, *4*, 7051.
(24) Guo, M.; He, J.; Li, Y.; Ma, S.; Sun, X. One-step Synthesis of Hollow Porous Gold Nanoparticles with Tunable Particle Size for the Reduction of 4-Nitrophenol. *J. Hazard. Mater.* **2016**, *310*, 89−97.
(25) Ihsan, A.; Katsiev, H.; Alyami, N.; Anjum, D. H.; Khan, W. S.; Hussain, I. From Porous Gold Nanocups to Porous Nanospheres and Solid Particles: a New Synthetic Approach. *J. Colloid Interface Sci.* **2015**, *446*, 59−66.
(26) Bahar, N.; Ekinci, D. Hollow porous gold nanoparticle/reduced graphene oxide composite films for electrochemical supercapacitor applications. *Electrochim. Acta* **2020**, *337*, 135844.
(27) Zielinski, M. S.; Choi, J.-W.; La Grange, T.; Modestino, M.; Hashemi, S. M. H.; Pu, Y.; Birkhold, S.; Hubbell, J. A.; Psaltis, D. Hollow mesoporous plasmonic nanoshells for enhanced solar vapor generation. *Nano Lett.* **2016**, *16*, 2159−2167.
(28) Valencia, F. J.; Ramírez, M.; Varas, A.; Rogan, J. Understanding the Stability of Hollow Nanoparticles with Polycrystalline Shells. *J. Phys. Chem. C* **2020**, *124*, 10143−10149.
(29) Depciuch, J.; Stec, M.; Maximenko, A.; Baran, J.; Parlinska-Wojtan, M. Temperature-Controlled Synthesis of Hollow, Porous Gold Nanoparticles with Wide Range Light Absorption. *J. Mater. Sci.* **2020**, *55*, 5257.
(30) Shukla, S.; Priscilla, A.; Banerjee, M.; Bhonde, R. R.; Ghatak, J.; Satyam, P.; Sastry, M. Porous Gold Nanospheres by Controlled Transmetalation Reaction: A Novel Material for Application in Cell Imaging. *Chem. Mater.* **2005**, *17*, 5000−5005.
(31) Jeong, S.; Kim, M.-W.; Jo, Y.-R.; Kim, N.-Y.; Kang, D.; Lee, S. Y.; Yim, S.-Y.; Kim, B.-J.; Kim, J. H. Hollow porous gold nanoshells with controlled nanojunctions for highly tunable plasmon resonances and intense field enhancements for surface-enhanced Raman scattering. *ACS Appl. Mater. Interfaces* **2019**, *11*, 44458−44465.
(32) Valencia, F. J.; González, R. I.; Valdivia, J. A.; Kiwi, M.; Bringa, E. M.; Rogan, J. Inducing Porosity on Hollow Nanoparticles by Hypervelocity Impacts. *J. Phys. Chem. C* **2017**, *121*, 17856−17861.
(33) Reyes, P. N.; Valencia, F. J.; Vega, H.; Ruestes, C.; Rogan, J.; Valdivia, J.; Kiwi, M. The Stability of Hollow Nanoparticles and the Simulation Temperature Ramp. *Inorg. Chem. Front.* **2018**, *5*, 1139−1144.
(34) Valencia, F. J.; González, R. I.; Tramontina, D.; Rogan, J.; Valdivia, J. A.; Kiwi, M.; Bringa, E. M. Hydrogen Storage in Palladium Hollow Nanoparticles. *J. Phys. Chem. C* **2016**, *120*, 23836.
(35) Allen, M.; Tildesley, D. *Computer Simulations of Liquids*; Clarendon Press; Oxford, U.K., 1987.
(36) Rappaport, D. E. *The Art of Molecular Dynamics Simulation*; Cambridge University Press: Cambridge, U.K., 1996.
(37) Frenkel, D.; Smit, B. *Understanding Molecular Simulations*; Academics Press: San Diego, CA, 1996.
(38) Plimpton, S. Fast Parallel Algorithms for Short-Range Molecular Dynamics. *J. Comput. Phys.* **1995**, *117*, 1−19.
(39) Daw, M. S.; Baskes, M. I. Embedded-atom method: Derivation and application to impurities, surfaces, and other defects in metals. *Phys. Rev. B: Condens. Matter Mater. Phys.* **1984**, *29*, 6443.
(40) Sheng, H.; Kramer, M.; Cadien, A.; Fujita, T.; Chen, M. Highly Optimized Embedded-Atom-Method Potentials for Fourteen fcc Metals. *Phys. Rev. B: Condens. Matter Mater. Phys.* **2011**, *83*, 134118.
(41) Castro-Palacio, J. C.; Ladutenko, K.; Prada, A.; González-Rubio, G.; Díaz-Núñez, P.; Guerrero-Martínez, A.; Fernández de Córdoba, P.; Kohanoff, J.; Perlado, J. M.; Peña-Rodríguez, O.; Rivera, A. Hollow Gold Nanoparticles Produced by Femtosecond Laser Irradiation. *J. Phys. Chem. Lett.* **2020**, *11*, 5108−5114.
(42) Jiang, S.; Zhang, Y.; Gan, Y.; Chen, Z.; Peng, H. Molecular dynamics study of neck growth in laser sintering of hollow silver nanoparticles with different heating rates. *J. Phys. D: Appl. Phys.* **2013**, *46*, 335302.
(43) Ferbonink, G.; Rodrigues, T. S.; Camargo, P.; Albuquerque, R.; Nome, R. Stochastic thermodynamics analysis of ultrafast AgAu nanoshell dynamics in the nonlinear response regime. *ChemRxiv*, DOI: 10.26434/chemrxiv.12846695.v1.
(44) Valencia, F. J.; Pinto, B.; Kiwi, M.; Ruestes, C. J.; Bringa, E. M.; Rogan, J. Nanoindentation of polycrystalline Pd hollow nanoparticles: Grain size role. *Comput. Mater. Sci.* **2020**, *179*, 109642.
(45) Sheng, H. W.; Kramer, M. J.; Cadien, A.; Fujita, T.; Chen, M. W. Highly Optimized Embedded-Atom-Method Potentials for

Fourteen fcc Metals. *Phys. Rev. B: Condens. Matter Mater. Phys.* **2011**, *83*, 134118.
(46) Bringa, E. M.; Caro, A.; Wang, Y.; Victoria, M.; McNaney, J.; Remington, B.; Smith, R.; Torralva, B.; Swygenhoven, H. V. Ultrahigh Strength in Nanocrystalline Materials Under Shock Loading. *Science* **2005**, *309*, 1838.
(47) Valencia, F.; Mella, J. D.; González, R. I.; Kiwi, M.; Bringa, E. M. Confinement Effects in Irradiation of Nanocrystalline Diamond. *Carbon* **2015**, *93*, 458−464.
(48) Valencia, F. J.; González, R. I.; Bringa, E. M.; Kiwi, M. Hillock Formation on Nanocrystalline Diamond. *Carbon* **2017**, *119*, 219−224.
(49) Stukowski, A. Visualization and Analysis of Atomistic Simulation Data with OVITO-the Open Visualization Tool. *Modell. Simul. Mater. Sci. Eng.* **2010**, *18*, 015012.
(50) Stukowski, A. Structure Identification Methods for Atomistic Simulations of Crystalline Materials. *Modell. Simul. Mater. Sci. Eng.* **2012**, *20*, 045021.
(51) Honeycutt, J. D.; Andersen, H. C. Molecular Dynamics Study of Melting and Freezing of Small Lennard-Jones Clusters. *J. Phys. Chem.* **1987**, *91*, 4950−4963.
(52) Heinz, H.; Vaia, R.; Farmer, B.; Naik, R. Accurate simulation of surfaces and interfaces of face-centered cubic metals using 12- 6 and 9- 6 Lennard-Jones potentials. *J. Phys. Chem. C* **2008**, *112*, 17281−17290.
(53) Geada, I. L.; Ramezani-Dakhel, H.; Jamil, T.; Sulpizi, M.; Heinz, H. Insight into induced charges at metal surfaces and biointerfaces using a polarizable Lennard−Jones potential. *Nat. Commun.* **2018**, *9*, 716.
(54) Heinz, H.; Lin, T.-J.; Kishore Mishra, R.; Emami, F. S. Thermodynamically consistent force fields for the assembly of inorganic, organic, and biological nanostructures: the INTERFACE force field. *Langmuir* **2013**, *29*, 1754−1765.
(55) Zhou, J.; Yang, Y.; Yang, Y.; Kim, D. S.; Yuan, A.; Tian, X.; Ophus, C.; Sun, F.; Schmid, A. K.; Nathanson, M.; Heinz, H.; An, Q.; Zeng, H.; Ercius, P.; Miao, J. Observing crystal nucleation in four dimensions using atomic electron tomography. *Nature* **2019**, *570*, 500−503.
(56) Nathanson, M.; Kanhaiya, K.; Pryor, A., Jr; Miao, J.; Heinz, H. Atomic-Scale structure and stress release mechanism dain core−shell nanoparticles. *ACS Nano* **2018**, *12*, 12296−12304.
(57) Avila-Salas, F.; González, R. I.; Ríos, P. L.; Araya-Durán, I.; Camarada, M. B. Effect of the Generation of PAMAM Dendrimers on the Stabilization of Gold Nanoparticles. *J. Chem. Inf. Model.* **2020**, *60*, 2966−2976.
(58) Simmons, G.; Wang, H. *Single crystal elastic constants and calculated aggregate properties*; MIT Press: Cambridge, MA, 1971.
(59) Lynn, J.; Smith, H.; Nicklow, R. Lattice dynamics of gold. *Phys. Rev. B* **1973**, *8*, 3493.
(60) Valencia, F. J.; González, R. I.; Vega, H.; Ruestes, C.; Rogan, J.; Valdivia, J. A.; Bringa, E. M.; Kiwi, M. Mechanical Properties Obtained by Indentation of Hollow Pd Nanoparticles. *J. Phys. Chem. C* **2018**, *122*, 25035−25042.
(61) Park, T.-H.; Jang, D.-J. Laser-induced fabrication of porous gold nanoshells. *Nanoscale* **2018**, *10*, 20108−20112.

https://dx.doi.org/10.1021/acs.jcim.0c00785
J. Chem. Inf. Model. 2020, 60, 6204−6210